View metadata, citation and similar papers at core.ac.uk
brought to you by CORE
provided by Okayama University Scientific Achievement Repository

PHYSICAL REVIEW B **95**, 245310 (2017)

Transistor properties of exfoliated single crystals of $2H$-$Mo(Se_{1-x}Te_x)_2$ ($0 \leqslant x \leqslant 1$)

Eri Uesugi,[1] Xiao Miao,[1] Hiromi Ota,[2] Hidenori Goto,[1] and Yoshihiro Kubozono[1,*]
[1]*Research Institute for Interdisciplinary Science, Okayama University, Okayama 700-8530, Japan*
[2]*Advanced Science Research Center, Okayama University, Okayama 700-8530, Japan*
(Received 17 January 2017; revised manuscript received 25 April 2017; published 15 June 2017)

Field-effect transistors (FETs) were fabricated using exfoliated single crystals of $Mo(Se_{1-x}Te_x)_2$ with an x range of 0 to 1, and the transistor properties fully investigated at 295 K in four-terminal measurement mode. The chemical composition and crystal structure of exfoliated single crystals were identified by energy-dispersive x-ray spectroscopy (EDX), single-crystal x-ray diffraction, and Raman scattering, suggesting the $2H$- structure in all $Mo(Se_{1-x}Te_x)_2$. The lattice constants of a and c increase monotonically with increasing x, indicating the substitution of Se by Te. When $x < 0.4$ in a FET with a thin single crystal of $Mo(Se_{1-x}Te_x)_2$, n-channel FET properties were observed, changing to p-channel or ambipolar operation for $x > 0.4$. In contrast, the polarity of a thick single-crystal $Mo(Se_{1-x}Te_x)_2$ FET did not change despite an increase in x. The change of polarity in a thin single-crystal FET was well explained by the variation of electronic structure. The absence of such change in the thick single-crystal FET can be reasonably interpreted based on the large bulk conduction due to naturally accumulated electrons. The μ value in the thin single-crystal FET showed a parabolic variation, with a minimum μ at around $x = 0.4$, which probably originates from the disorder of the single crystal caused by the partial replacement of Se by Te, i.e., a disorder that may be due to ionic size difference of Se and Te.

DOI: 10.1103/PhysRevB.95.245310

I. INTRODUCTION

Transition-metal dichalcogenides (TMDs) are of great interest to physicists and chemists because they have recently produced new and exciting physics, as well as potentially useful materials for future electronics [1–16]. Pressure-driven superconductivity [4–6], large magnetoresistance [7], and a large Nernst effect [8] have been observed in some TMDs, and a possible Weyl semimetal [9] and a two-dimensional topological insulator [10] are also being discussed. Furthermore, because the TMDs are layer network materials with strong covalent bonds in a layerlike graphene, which may lead to high carrier transport, i.e., high field-effect mobility μ, the application of TMDs in field-effect transistors (FETs) has been systematically pursued [11–13]. All TMDs have a significant band gap, which may be more suitable for FET application than graphene without a band gap because of the easy switching of channel transport. As described later, the features of electronic structures in TMDs can be tuned via a change in the number of layers, i.e., the band gap can be also controlled. In addition, a technique of exfoliation available for graphene can easily be used on TMD compounds. The weak van der Waals interaction between layers in TMDs allows the intercalation of various elements and molecules [14–16], providing a fascinating platform for exploration in physics and materials science.

$MoSe_2$ and $MoTe_2$ are representative TMDs, and their physical and chemical properties have been extensively investigated [17–20]. Crystals of $MoSe_2$ and $MoTe_2$ have four polymorphs, called $2H$, $1T$, $1T'$, and T_d. Of these crystal types, the $2H$ and $1T$ are semiconducting, while the $1T'$ and T_d are semimetallic. The band gap in bulk $2H$-$MoSe_2$ is reported to be 1.1 eV [21], while the gap in bulk $2H$-$MoTe_2$ is 1.0 eV [22]. The indirect band gap corresponds to $[\Gamma - (\Gamma\ K)]$, where $(\Gamma\ K)$ means an intermediate state between Γ and K points [22]. Single layers of $MoSe_2$ or $MoTe_2$ exhibit a direct K-K band gap of 1.58 and 1.23 eV, respectively [22]. The band gap is tuned by modifying the number of layers in $MoSe_2$ and $MoTe_2$.

Recently, T_d-$MoTe_2$ was predicted to be a Weyl semimetal [9], and showed superconductivity with a transition temperature T_c of 0.10 K [6]. The T_d-$MoTe_2$ crystal was obtained via a $1T'$-T_d first-order structural transition by cooling a $1T'$ crystal. Under applied pressure, this first-order transition of the $1T'$-$MoTe_2$ crystal disappeared, and high-T_c superconductivity was suddenly observed, with a maximum T_c of 8.2 K at 11.7 GPa [6]. Pressure-driven superconductivity is also observed in WTe_2 [4], which exhibits a T_c as high as 7 K at 16.8 GPa. Metal intercalation in MoS_2 and $MoSe_2$ yielded superconductivity with $T_c \sim 4-7$ K [14–16]. Metal intercalation has been achieved using the liquid ammonia (NH_3) method. Therefore, the metal atoms are codoped together with NH_3 or an amide, i.e., the MoS_2 and $MoSe_2$ compounds can provide a good intercalation space for metal atoms and molecules [16]. As described above, this originates in the weak interaction between layers. Electrostatic carrier doping has been achieved in MoS_2 and $MoSe_2$ [23,24], providing a domelike T_c-n phase diagram, where n is electron density.

Single crystals and thin films of $MoSe_2$ and $MoTe_2$ have been fully investigated from the viewpoint of transistor application [25–28]. Various gate dielectrics have been used for the above single-crystal and thin-film FETs. The maximum μ value for a $MoSe_2$ single-crystal FET is currently $\sim 50\ cm^2\ V^{-1}\ s^{-1}$ at room temperature when using a SiO_2 gate dielectric [25,26]. On the other hand, the μ values of $MoTe_2$ single-crystal FETs are $\sim 20\ cm^2\ V^{-1}\ s^{-1}$ for the SiO_2 gate dielectric [27], and $26\ cm^2\ V^{-1}\ s^{-1}$ for the ionic liquid [28]. The μ value is lower than that in a graphene FET (more than $10^4\ cm^2\ V^{-1}\ s^{-1}$ at room temperature [29]). Nevertheless, the on-off ratio of channel transport is more than 10^6, which is much higher than that in a normal graphene FET. Therefore,

*Corresponding author: kubozono@cc.okayama-u.ac.jp

 ©2017 American Physical Society

TABLE I. Temperatures used for single-crystal growth.

Nominal x	Low-temperature zone	High-temperature zone
0	900 °C	1000 °C
0.25	800 °C	900 °C
0.4–1	700 °C	800 °C

$MoSe_2$ and $MoTe_2$ single-crystal FETs are very attractive for future practical devices such as high-speed logic gate circuits. In this paper, we have systematically investigated the characteristics of $Mo(Se_{1-x}Te_x)_2$ single-crystal FETs with x values of 0 to 1. All single crystals were assigned to the $2H$ structure. The FET devices were fabricated using well-defined crystals of $2H$-$Mo(Se_{1-x}Te_x)_2$ with two different thicknesses, to determine the thickness dependence of their FET characteristics, since their electronic structures may be tuned by changing the number of layers. To the best of our knowledge, the FET properties have not yet been determined for a series of $2H$-$Mo(Se_{1-x}Te_x)_2$ single crystals with uniform thickness. In this study, we have systematically recorded the FET characteristics in four-terminal measurement mode for $2H$-$Mo(Se_{1-x}Te_x)_2$ single-crystal FETs with different thicknesses, which led to not only a continuous tuning of FET properties by changing the amount of Te, but a clear observation of polarity switching.

II. EXPERIMENTAL

Single crystals of $Mo(Se_{1-x}Te_x)_2$ were formed from polycrystalline powder $Mo(Se_{1-x}Te_x)_2$ samples by chemical vapor transport using a furnace with different temperature zones [30]; powder $Mo(Se_{1-x}Te_x)_2$ samples were prepared by annealing stoichiometric amounts of Mo, Se, and Te powder at 800 °C for 5 d and then 1000 °C for 5 d using a procedure reported elsewhere [30]. $TeCl_4$ was mixed with a $Mo(Se_{1-x}Te_x)_2$ sample as a transport material for preparing single crystals of $Mo(Se_{1-x}Te_x)_2$. Each $Mo(Se_{1-x}Te_x)_2$ powder sample was set in the high-temperature zone, and its single crystal was collected in the low-temperature zone; the temperature for each zone is listed in Table I. The energy-dispersive x-ray spectroscopy (EDX) spectrum was measured with an EDX spectrometer equipped with a scanning electron microscope (KEYENCE VE-9800 - EDAX Genesis XM2). Single-crystal x-ray diffraction (XRD) measurement was performed at 100 K using a Rigaku Saturn 724 diffractometer equipped with a Mo $K\alpha$ source (wavelength $\lambda = 0.710\ 75$ Å). Raman spectra were measured at room temperature using a JASCO NRS-3100 Raman spectrometer.

The value of sheet conductivity σ_s was determined from the slope (or R) derived by linear fitting of the V-I plots in four-terminal measurement mode; details are described later. In these measurements, the I was applied with a Keithley 2636A sourcemeter. The V was measured with an Advantest R6871E digital multimeter and a Preamplifier 1201 (DL Instruments, LLC). The V_g was applied to a heavily doped Si substrate for the $Mo(Se_{1-x}Te_x)_2$ single-crystal FET with 300-nm-thick SiO_2 gate dielectric using a Keithley 2636A sourcemeter. The device structure (top-contact type) is illustrated in Fig. 3(a); top-contact electrodes were formed by 110-nm-thick Au, and 5 nm Cr was inserted between the Au electrode and the single crystal. The electrode pattern was designed using photolithography (Kyowa Riken, K-309PW95) or electron beam lithography equipment (Elionix, EBL-S50).

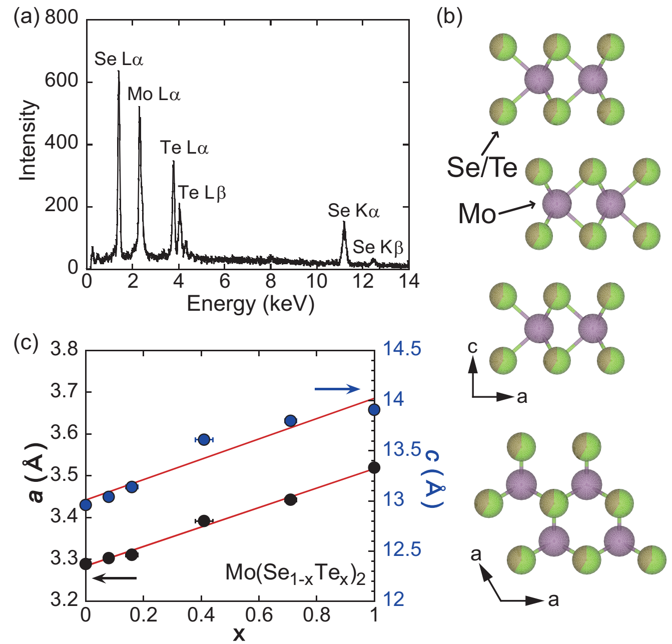

FIG. 1. (a) EDX spectrum of $Mo(Se_{0.5}Te_{0.5})_2$; the chemical composition of this sample is the experimental nominal value. (b) Schematic representation of crystal structure of $2H$-$Mo(Se_{1-x}Te_x)_2$. (c) Lattice constants, a and c, as a function of x in $2H$-$Mo(Se_{1-x}Te_x)_2$; the x value was determined from single-crystal x-ray diffraction analysis. Error bars for x, a, and c are shown. Red lines are fitted as linear.

III. RESULTS AND DISCUSSION

A. Characterization of single crystals of $Mo(Se_{1-x}Te_x)_2$

The stoichiometry of $Mo(Se_{1-x}Te_x)_2$ crystals was determined using EDX. As an example, the EDX spectrum of $Mo(Se_{1-x}Te_x)_2$ at $x = 0.5$ [$Mo(Se_{0.5}Te_{0.5})_2$] is shown in Fig. 1(a). All peaks observed could be assigned to Mo, Se, and Te, and the chemical stoichiometry of the crystal was determined to be $Mo(Se_{0.65(3)}Te_{0.44(9)})_2$. Single-crystal x-ray diffraction analysis of each $Mo(Se_{1-x}Te_x)_2$ crystal was performed to determine its stoichiometry and crystal structure. Analyses of single-crystal diffraction data clearly showed that all crystals used in this study had a $2H$ structure [space group of $P6_3/mmc$ (no. 194)]. The stoichiometry of $Mo(Se_{0.5}Te_{0.5})_2$ was determined to be $Mo(Se_{0.59(3)}Te_{0.41(3)})_2$, and lattice constants a and c of $Mo(Se_{0.5}Te_{0.5})_2$ were 3.392(7) and 13.61(3) Å, respectively; the amounts of Se and Te were determined under the constraint that the total number of moles of Se and Te was 2. The stoichiometry, $Mo(Se_{0.59(3)}Te_{0.41(3)})_2$, is consistent with the $Mo(Se_{0.65(3)}Te_{0.44(9)})_2$ determined from the EDX spectra, in which the stoichiometry of Se and Te was expressed with respect to 1 mol of Mo. The crystallographic data for $Mo(Se_{0.5}Te_{0.5})_2$ are listed in Table II. As can

TABLE II. Crystallographic data of $Mo(Se_{0.5}Te_{0.5})_2$.

Site		Occ.	x	y	z	B(Å^2)
2c	Mo	1.00	0.33333	0.66667	0.25000	0.50(7)
4f	Se	0.59(3)	0.33333	0.66667	0.6207(1)	0.90(5)
4f	Te	0.41(3)	0.33333	0.66667	0.6207(1)	0.90(5)

be seen in the crystal structure shown in Fig. 1(b), the $Mo(Se_{0.59(3)}Te_{0.41(3)})_2$ layer is stacked along the c axis.

Table III lists the stoichiometry and lattice constants, z of the 4f site, and the B value of a Se(Te) atom for each $Mo(Se_{1-x}Te_x)_2$ crystal, determined from single-crystal x-ray diffraction together with the stoichiometry from EDX. Throughout this paper, the chemical formula is expressed based on the crystallographic data determined by single-crystal x-ray diffraction. As seen in Fig. 1(c), a and c increase monotonically with increasing x, which is plotted as a function of the x value determined from single-crystal x-ray diffraction. The graph shown in Fig. 1(c) shows that all lattice constants lie on the straightforward lines connecting those of $MoSe_2$ and $MoTe_2$, implying that each stoichiometry determination by x-ray diffraction was reliable.

To identify the structure of $Mo(Se_{1-x}Te_x)_2$ crystals, Raman spectra of thin single crystals were measured using an excitation energy of 488 nm. All Raman spectra are plotted in Fig. 2, where characteristic peaks at 250 and 290 cm^{-1} are observed in a thin $MoSe_2$ single crystal, showing that it is a 2H-crystal, as indicated in Ref. [31]. These peaks can be assigned to A_{1g} and E_{2g} Raman active modes. On the other hand, the characteristic peaks at 175 and 235 cm^{-1} are observed in $MoTe_2$, showing that it is also a 2H-crystal. These peaks can also be assigned to A_{1g} and E_{2g} Raman active modes. The peak at 255 cm^{-1} in $Mo(Se_{0.59(3)}Te_{0.41(3)})_2$ single crystal can be assigned to an E_{2g} peak, which is located between 235 cm^{-1} ($MoTe_2$) and 290 cm^{-1} ($MoSe_2$). This indicates that Se atoms have been replaced by Te, and the crystal structure is 2H for all $Mo(Se_{1-x}Te_x)_2$ single crystals.

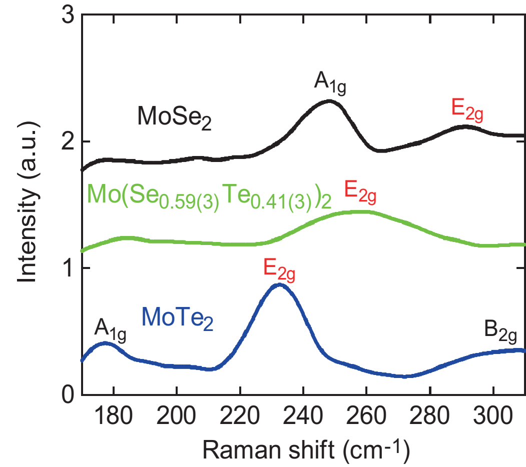

FIG. 2. Raman spectra of 2H-$Mo(Se_{1-x}Te_x)_2$.

B. Polarity switching in $Mo(Se_{1-x}Te_x)_2$ thin single-crystal FET

A schematic representation of FET devices fabricated using single crystals of $Mo(Se_{1-x}Te_x)_2$ is shown in Fig. 3(a). $Mo(Se_{1-x}Te_x)_2$ crystals with different thicknesses (5–15 nm and 30–100 nm) are used for the active layer of the FET. Throughout this paper, 5–15-nm-thick crystal is called “thin single crystal,” while 30–100-nm-thick crystal is called “bulk (or thick) single crystal.” The gate dielectric is 300-nm-thick SiO_2. Figures 3(b)–3(g) show sheet conductivity $\sigma_s = [(dI/dV) \times (L/W)]$ as a function of gate voltage V_g in a FET with a thin single crystal of $Mo(Se_{1-x}Te_x)_2$ ($x = 0 - 1$). The channel length and channel width are shown in Fig. 3(a).

Figure 3(e) shows the σ_s-V_g plot for $Mo(Se_{0.59(3)}Te_{0.41(3)})_2$ (thickness = 5.0 nm) thin single-crystal FET. As seen from Fig. 3(e), clear p-channel operation is observed in the σ_s-V_g plot in the $Mo(Se_{0.59(3)}Te_{0.41(3)})_2$ thin single-crystal FET, which means that $x = 0.41$. The field-effect mobility μ and threshold voltage V_{th} were evaluated to be 4.4 cm^2 V^{-1} s^{-1} and −12 V, respectively, showing p-channel normally off FET properties. The μ is smaller than the ∼50 cm^2 V^{-1} s^{-1} reported in FETs with thin single crystals of $MoSe_2$, and the operation type [p channel for $Mo(Se_{1-x}Te_x)_2$ at $x = 0.41$] is in contrast to the n-channel FET properties of $MoSe_2$ ($x = 0$) [25]. On the other hand, p-channel operation is consistent with that of a $MoTe_2$ thin single-crystal FET ($x = 1$) [27]. At $x = 1$, we also observed ambipolar (n- and p-channel) FET modes or p-channel FET mode, as seen in Fig. 3(h), in which the p-channel μ value taken from Ref. [27] is plotted. On the other hand, the n-channel mode was observed at $x = 0.71$. The behavior at $x = 0.71$ is different from that at $x = 0.41$ and 1, but the n-channel property at $x = 0.71$ is poorer than those around $x = 0$. As a result, it can be concluded that the operating mode tends to change to p channel as values of x increase. In Fig. 3(h), the μ values for $MoSe_2$ FET taken from Refs. [25] and [26] are also plotted.

TABLE III. Stoichiometry, lattice constants, z of 4f site, and B value of Se(Te) atoms for each $Mo(Se_{1-x}Te_x)_2$ crystal, as determined from single-crystal x-ray diffraction, with stoichiometry from EDX.

Nominal x	EDX	XRD	a (Å)	c (Å)	z of 4f	B (Å^2)
0	$MoSe_{2.4(3)}$	$MoSe_2$	3.289(7)	12.96(3)	0.62096(8)	0.26(3)
0.25	$Mo(Se_{0.96(3)}Te_{0.22(2)})_2$	$Mo(Se_{0.85(2)}Te_{0.16(2)})_2$	3.311(6)	13.14(2)	0.6210(1)	0.72(4)
0.4	$Mo(Se_{1.065(5)}Te_{0.070(5)})_2$	$Mo(Se_{0.91(1)}Te_{0.08(1)})_2$	3.303(2)	13.04(1)	0.62102(8)	0.39(3)
0.5	$Mo(Se_{0.65(3)}Te_{0.44(9)})_2$	$Mo(Se_{0.59(3)}Te_{0.41(3)})_2$	3.392(7)	13.61(3)	0.6207(1)	0.90(5)
0.9	$Mo(Se_{0.3(1)}Te_{0.4(1)})_2$	$Mo(Se_{0.29(2)}Te_{0.71(2)})_2$	3.443(5)	13.80(2)	0.6206(1)	0.81(4)
1	$MoTe_{1.85(5)}$	$MoTe_2$	3.520(7)	13.91(3)	0.62034(5)	0.30(4)

FIG. 3. (a) Device structure of $2H$-Mo$(\mathrm{Se}_{1-x}\mathrm{Te}_x)_2$ single-crystal FET. (b)–(g) σ_s-V_g plots for thin single-crystal FETs with $2H$-Mo$(\mathrm{Se}_{1-x}\mathrm{Te}_x)_2$ at $x = 0 - 1$; x value is shown in each graph. The x value was determined from single-crystal x-ray diffraction. Red lines are fitted as linear in (b)–(g). (h) μ-x plot from $2H$-Mo$(\mathrm{Se}_{1-x}\mathrm{Te}_x)_2$ thin single-crystal FET; x was determined from single-crystal x-ray diffraction. Solid and open symbols refer to experimental μ values found in this study, and those taken from Refs. [25–27], respectively. Dashed curve is an eye guide.

The μ value for n-channel normally on operation decreases with increasing amounts of Te (x) and changes to p-channel normally off operation at $x = 0.41$ [see Figs. 3(b)–3(g)]. The decrease in μ for materials that incorporate both Se and Te may be simply explained by the increase in the disorder of the Se(Te) presence at the $4f$ site of single crystals. Figure 4 shows a plot of the Debye-Waller factor (B) versus x, suggesting an increase in disorder for $0 < x < 1$ in Mo$(\mathrm{Se}_{1-x}\mathrm{Te}_x)_2$ because the B values are larger than those at $x = 0$ and $x = 1$; B is an indication of static disorder in the pattern of the Se/Te atoms. On the other hand, to explain the change of FET polarity from n- to p channel (or ambipolarity), we must consider the electronic properties of $2H$ thin single crystals of MoSe_2 and MoTe_2. Furthermore, it should be noted that normally on properties are observed for n-channel operation in the small-x range, indicative of the naturally accumulated electrons in Mo$(\mathrm{Se}_{1-x}\mathrm{Te}_x)_2$ with small values of x, i.e., samples with only a small amount of Te.

The n-channel FET mode in a MoSe_2 single-crystal FET can be well explained by the fact that the Fermi level in a

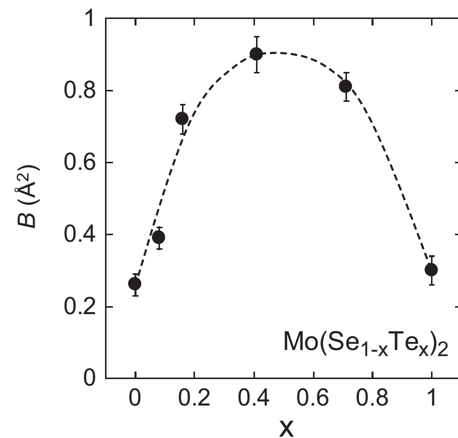

FIG. 4. B-x plot from $2H$-Mo$(\mathrm{Se}_{1-x}\mathrm{Te}_x)_2$ single crystal; x was determined from single-crystal x-ray diffraction. B refers to the Debye-Waller factor of Se(Te) atom at $4f$ site. Dashed curve is an eye guide.

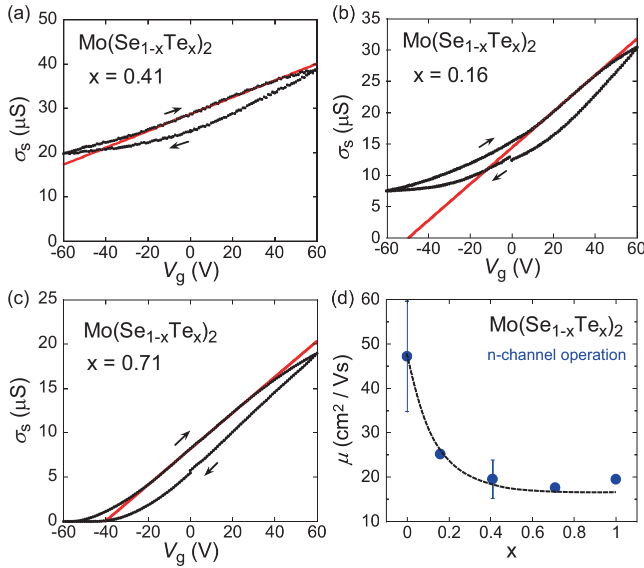

FIG. 5. σ_s-V_g plots for thick single-crystal FET with $2H$-$Mo(Se_{1-x}Te_x)_2$ at (a) $x = 0.41$, (b) $x = 0.16$, and (c) $x = 0.71$, as determined from single-crystal x-ray diffraction. Red lines are fitted as linear in (a)–(c). (d) μ-x plot in $2H$-$Mo(Se_{1-x}Te_x)_2$ thick single-crystal FET; x was determined from single-crystal x-ray diffraction. Dashed curve is an eye guide.

monolayer of $2H$-$MoSe_2$ crystal is closer to the bottom of the conduction band (K point) than the top of the valence band (K point) [22]. In contrast, the energy difference between the bottom of the conduction band (K point) and the Fermi level in a monolayer of $2H$-$MoTe_2$ crystal is the same as that between the top of the valence band (K point) and the Fermi level [22]. This explains well the ambipolar FET property of a $MoTe_2$ thin single-crystal FET. We often observed weak n-channel FET characteristics as well as p-channel properties in a $MoTe_2$ single-crystal FET.

C. Transistor properties of $Mo(Se_{1-x}Te_x)_2$ thick single-crystal FETs

The FET properties of $Mo(Se_{1-x}Te_x)_2$ thick single-crystal FETs with 300-nm-thick SiO_2 gate dielectrics were compared with those of thin single-crystal FETs. As shown in Fig. 5(a), clear n-channel normally on operation (depletion-type characteristics) is observed in the σ_s-V_g plot for a $Mo(Se_{0.59(3)}Te_{0.41(3)})_2$ thick single-crystal FET ($x = 0.41$), which is in contrast to that of a thin single-crystal FET; the thickness of the single crystal was 67 nm. The μ and V_{th} were determined to be 16.5 $cm^2\,V^{-1}\,s^{-1}$ and -150 V, respectively, from the transfer curve [Fig. 5(a)]. Typical σ_s-V_g plots for $Mo(Se_{1-x}Te_x)_2$ thick single-crystal FETs ($x = 0 - 1$) are shown in Figs. 5(b) and 5(c), exhibiting only n-channel normally on properties; the σ_s values at $V_g = 0$ V in thick single-crystal FETs are higher than those of thin single-crystal FETs even in the small-x range, indicating that the bulk crystal contains a significant quantity of accumulated electrons. The absence of a polarity change from n- to p-channel operation with varying x in a thick single-crystal FET [Fig. 5(d)] indicates that the electrostatic depletion of electrons in the channel region cannot completely suppress bulk conduction by electrons. In other words, bulk electron conduction dominates in the bulk crystal of $2H$-$Mo(Se_{1-x}Te_x)_2$, which leads to solely n-channel transport in those FETs.

IV. SUMMARY AND OUTLOOK

The transport properties of thin and thick $2H$-$Mo(Se_{1-x}Te_x)_2$ single-crystal FETs were systematically investigated in an x range of 0 to 1. The polarity of FET characteristics changed from n- to p channel (or ambipolar) for thin $2H$-$Mo(Se_{1-x}Te_x)_2$ single-crystal FETs with increasing x, while the polarity did not change for thick $Mo(Se_{1-x}Te_x)_2$ single-crystal FETs. The change of polarity in thin single-crystal FETs was reasonably explained based on the electronic structures of $MoSe_2$ and $MoTe_2$, and the absence of change in thick single-crystal FET was explained based on the presence of large bulk conductance ascribable to naturally accumulated electrons. The μ value decreased with the replacement of Se by Te. At around $x = 0.4$, the μ value reached a minimum for thin single-crystal FETs. This result was well explained by the disorder in the crystal, as evidenced by the increase in B of Se(Te) atoms at the $4f$ site. In this paper, the most important issue is that the amount of Te in the semiconducting $2H$-$Mo(Se_{1-x}Te_x)_2$ crystal provided two contributions, polarity change and parabolic variation of the μ value, for the thin single-crystal FET, i.e., the former is caused by variation of the electronic structure, while the latter is caused by the disorder in the crystals due to the different ionic sizes of Se^{2-} (1.98 Å) and Te^{2-} (2.21 Å). The p-n polarity change and the parabolic x dependence of μ were not observed in thick single-crystal FETs because of the large contribution from bulk transport. To sum up, the successful tuning of FET properties, including polarity switching, by controlling the chemical composition of single-crystal $Mo(Se_{1-x}Te_x)_2$ provided significant fundamental information to guide the use of exfoliated single-crystal $Mo(Se_{1-x}Te_x)_2$ in future tailor-made electronics.

ACKNOWLEDGMENTS

This study was partly supported by Grants-in-Aid (26105004, 26400361, and 26000228) from MEXT, by the ACT-C program of JST, and by the Program for Promoting the Enhancement of Research Universities.

[1] Y. J. Zhang, T. Oka, R. Suzuki, J. T. Ye, and Y. Iwasa, Science **344**, 725 (2014).
[2] X. Xu, W. Yao, D. Xiao, and T. F. Heinz, Nat. Phys. **10**, 343 (2014).
[3] R. A. Klemm, Physica C **514**, 86 (2015).
[4] X.-C. Pan, X. Chen, H. Liu, Y. Feng, Z. Wei, Y. Zhou, Z. Chi, L. Pi, F. Yen, F. Song, X. Wan, Z. Yang, B. Wang, G. Wang, and Y. Zhang, Nat. Commun. **6**, 7805 (2015).
[5] B. Sipos, A. F. Kusmartseva, A. Akrap, H. Berger, L. Ferró, and E. Tuti, Nat. Mater. **7**, 960 (2008).

[6] Y. Qi, P. G. Naumov, M. N. Ali, C. R. Rajamathi, W. Schnelle, O. Barkalov, M. Hanfland, S.-C. Wu, C. Shekhar, Y. Sun, V. Süß, M. Schmidt, U. Schwarz, E. Pippel, P. Werner, R. Hillebrand, T. Förster, E. Kampert, S. Parkin, R. J. Cava, C. Felser, B. Yan, and S. A. Medvedev, Nat. Commun. **7**, 11038 (2016).
[7] M. N. Ali, J. Xiong, S. Flynn, J. Tao, Q. D. Gibson, L. M. Schoop, T. Liang, N. Haldolaarachchige, M. Hirschberger, N. P. Ong, and R. J. Cava, Nature (London) **514**, 205 (2014).
[8] Z. Zhu, X. Lin, J. Liu, B. Fauqué, Q. Tao, C. Yang, Y. Shi, and K. Behnia, Phys. Rev. Lett. **114**, 176601 (2015).
[9] Y. Sun, S.-C. Wu, M. N. Ali, C. Felser, and B. Yan, Phys. Rev. B **92**, 161107(R) (2015).
[10] X. Qian, J. Liu, L. Fu, and J. Li, Science **346**, 1344 (2014).
[11] H.-J. Chuang, X. Tan, N. J. Ghimire, M. M. Perera, B. Chamlagain, M. M.-C. Cheng, J. Yan, D. Mandrus, D. Tománek, and Z. Zhou, Nano Lett. **14**, 3594 (2014).
[12] Y.-F. Lin, Y. Xu, S.-T. Wang, S.-L. Li, M. Yamamoto, A. Aparecido-Ferreira, W. Li, H. Sun, S. Nakaharai, W.-B. Jian, K. Ueno, and K. Tsukagoshi, Adv. Mater. **26**, 3263 (2014).
[13] K. Choi, Y. T. Lee, J. S. Kim, S.-W. Min, Y. Cho, A. Pezeshki, D. K. Hwang, and S. Im, Adv. Funct. Mater. **26**, 3146 (2016).
[14] G. V. Subba Rao, M. W. Shafer, S. Kawarazaki, and A. M. Toxen, J. Solid State Chem. **9**, 323 (1974).
[15] J. A. Woollam and R. B. Somoano, Mater. Sci. Eng. **31**, 289 (1977).
[16] X. Miao, S. Nishiyama, L. Zheng, H. Goto, R. Eguchi, H. Ota, T. Kambe, K. Terashima, T. Yokoya, H. T. L. Nguyen, T. Kagayama, N. Hirao, Y. Ohishi, H. Ishii, Y.-F. Liao, and Y. Kubozono, Sci. Rep. **6**, 29292 (2016).
[17] M. Riflikova, R. Martoňák, and E. Tosatti, Phys. Rev. B **90**, 035108 (2014).
[18] L. Zhou, K. Xu, A. Zubair, A. D. Liao, W. Fang, F. Ouyang, Y.-H. Lee, K. Ueno, R. Saito, T. Palacios, J. Kong, and M. S. Dresselhaus. J. Am. Chem. Soc. **137**, 11892 (2015).
[19] A. Ambrosi, Z. Sofe, and M. Pumera, Chem. Commun. **51**, 8450 (2015).
[20] K. Ueno and K. Fukushima, Appl. Phys. Express **8**, 095201 (2015).
[21] T. Böker, R. Severin, A. Müller, C. Janowitz, R. Manzke, D. Voß, P. Krüger, A. Mazur, and J. Pollmann, Phys. Rev. B **64**, 235305 (2001).
[22] A. Kumar and P. K. Ahluwalia, Eur. Phys. J. B **85**, 186 (2012).
[23] J. T. Ye, Y. J. Zhang, R. Akashi, M. S. Bahramy, R. Arita, and Y. Iwasa, Science **338**, 1193 (2012).
[24] W. Shi, J. T. Ye, Y. J. Zhang, R. Suzuki, M. Yoshida, J. Miyazaki, N. Inoue, Y. Saito, and Y. Iwasa, Sci. Rep. **5**, 12534 (2015).
[25] B. Chamlagain, Q. Li, N. J. Ghimire, H.-J. Chuang, M. M. Perera, H. Tu, Y. Xu, M. Pan, D. Xaio, J. Yan, D. Mandrus, and Z. Zhou, ACS Nano **8**, 5079 (2014).
[26] S. Larentis, B. Fallahazad, and E. Tutuc, Appl. Phys. Lett. **101**, 223104 (2012).
[27] N. R. Pradhan, D. Rhodes, S. Feng, Y. Xin, S. Memaran, B.-H. Moon, H. Terrones, M. Terrones, and L. Balicas, ACS Nano **8**, 5911 (2014).
[28] H. Xu, S. Fathipour, E. W. Kinder, A. C. Seabaugh, and S. K. Fullerton-Shirey, ACS Nano **9**, 4900 (2015).
[29] K. S. Novoselov, A. K. Geim, S. V. Morozov, D. Jiang, Y. Zhang, S. V. Dubonos, I. V. Grigorieva, and A. A. Firsov, Science **306**, 666 (2004).
[30] M. Bougouma, A. Batan, B. Guel, T. Segato, J. B. Legma, F. Reniers, M.-P. Delplancke-Ogletree, B. Buess-Herman, and T. Doneux, J. Cryst. Growth **363**, 122 (2013).
[31] A. Roy, H. C. P. Mowa, B. Satpati, K. Kim, R. Dey, A. Rai, T. Pramanik, S. Guchhait, E. Tutuc, and S. K. Banerjee, ACS Appl. Mater. Interfaces **8**, 7396 (2016).